STUDY OF LOCAL DEFORMATION IN AN ADDITIVELY MANUFACTURED STEEL COMPOSITE

M. V. Nadezhkin, D. V. Orlova, and S. A. Barannikova   UDC 539.213; 669.017

The kinetics of localized deformation has been studied in a low-carbon steel/austenitic stainless steel composite produced by electron beam additive manufacturing. It is shown that the stress-strain curve of the bimetal is described by a parabolic law. Plastic deformation in all composite layers is localized according to the curve stages. First, a stationary dissipative system of localized plasticity foci is formed at the parabolic hardening stage with n = 0.5. At n ≤ 0.5, a high-amplitude deformation zone is observed in the transition layer, where a fracture eventually occurs in the specimen.

INTRODUCTION

Advances in additive manufacturing (AM) of metallic alloys have renewed interest in joining austenitic stainless steels. Additive manufacturing implies layer-by-layer formation of parts by melting powder or wire with a laser or electron beam heat source [1]. By varying the process parameters (laser power, components, and powder feed rate), composites with desired properties can be fabricated. There are sufficient microscopic studies on the phase formation in austenitic solidifying stainless steels (for example, see works [2–4]). However, macroscopic deformation mechanisms and strain localization should also be studied due to numerous discontinuities in AM parts. Digital image correlation (DIC) has been successfully applied for specimen examination in mechanical tests [5, 6], including for AM materials [7, 8]. Basically, the deformation behavior is studied on AM specimens cut along different direction, without taking into account the substrate interface. In this work, the strain field components are determined in the transition region between a low-carbon steel substrate and layers of austenitic stainless steel deposited along the tensile axis.

Previous studies showed that even single crystals and structurally homogeneous materials under loading are prone to the formation of localized deformation zones [9, 10]. Depending on the plastic flow stage, macroscopic plastic strain localization can occur as a switching wave in the case of Lüders banding, or a stationary periodic distribution pattern of localization zones at the parabolic hardening stage, or the autowave collapse at the prefracture stage [9]. Therefore, it is important to understand the kinetics of plastic strain localization in composites of two or more materials produced by additive manufacturing. Here we determine the kinetics of plastic strain macrolocalization during tension of a low-carbon steel/stainless steel composite obtained by electron beam wire feed additive manufacturing

MATERIALS AND METHODS

The studied material was the steel composite obtained from a 4-mm thick low-carbon steel sheet with a 5.5-mm thick layer of 308L austenitic stainless steel deposited in several passes by vacuum electron beam additive

---

Institute of Strength Physics and Materials Science of the Siberian Branch of the Russian Academy of Sciences, Tomsk, Russia, e-mail: dvo@ispms.ru; bsa@ispms.ru. Original article submitted June 16, 2023.

TABLE 1. Composition of Starting Materials

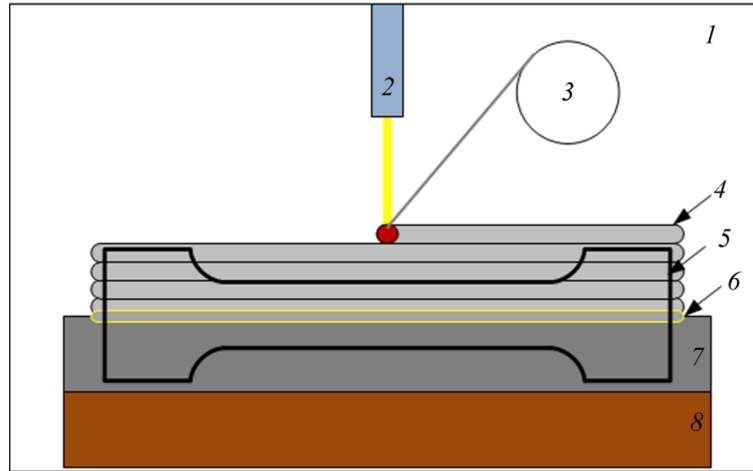|	C	Si	Mn	Ni	Cr	S	P	Fe
Substrate	0.14–0.22	0.12–0.3	0.4–0.65	< 0.3	< 0.3	< 0.05	< 0.04	Balance
Deposited layer	< 0.04	< 1.0	0.5–2.5	9.0–12.0	18.0–21.0	< 0.04	< 0.035	Balance

Fig. 1. Electron beam additive manufacturing scheme comprising vacuum chamber *1*, electron beam gun with electron beam *2*, wire feeder *3* with stainless steel, additive layer *4*, scheme of cutting a sample for testing *5*, transition layer *6*, substrate *7*, and copper plate *8* with water cooling.

manufacturing using a 1.6-mm diameter wire at the accelerator voltage $U_{ac} = 27$ kV, accelerator current $I = 60$ mA, wire feed rate $F = 3.8 \cdot 10^{-3}$ m/s, and a feed ratio of 1.3. The chemical composition of the materials is given in Table 1.

Dumbbell-shaped test specimens with gauge dimensions $40 \times 8.5 \times 2$ mm were cut by electric spark cutting perpendicularly to the substrate so that the deformation pattern could be observed in both layers on the side face of the specimen (Fig. 1).

Uniaxial tensile tests were conducted at room temperature on an LFM-125 testing machine (Walter + Bai AG). The movable grip velocity was $V_{mach} = 0.2$ mm/min to provide a strain rate of 8.33×10^{-5} s^{-1}. Strain localization zones were identified using sequentially recorded digital images of the deformed specimen. Speckle patterns were generated under coherent light illumination with a semiconductor laser (635 nm and 15.0 mW). The specimen was photographed using a Point Grey FL3-GE-50S5MC camera with a 2448×2048 pixel resolution at 5 fps. The camera was placed at a distance of 0.3 m from the specimen and gave a resolution of 20.4 µm/pixel. The images were processed *a posteriori* by DIC [5] to measure field displacements, strain components, and strain rates. Microstructural examination was performed by optical microscopy. The volume fraction of the ferromagnetic phase was determined by magnetization measurements on an MVP-2M multifunctional eddy current instrument.

RESULTS AND DISCUSSION

Microstructure and mechanical properties

Figure 2 shows the heterogeneous microstructure and the diagram of a bimetal specimen with characteristic areas. The substrate material exhibits ferrite grains with an average size of 10.9 ± 1.1 µm and pearlite. The typical microstructures of AM austenitic steels are two-phase, consisting of light γ-austenite and dark δ-ferrite [2, 3]. After the
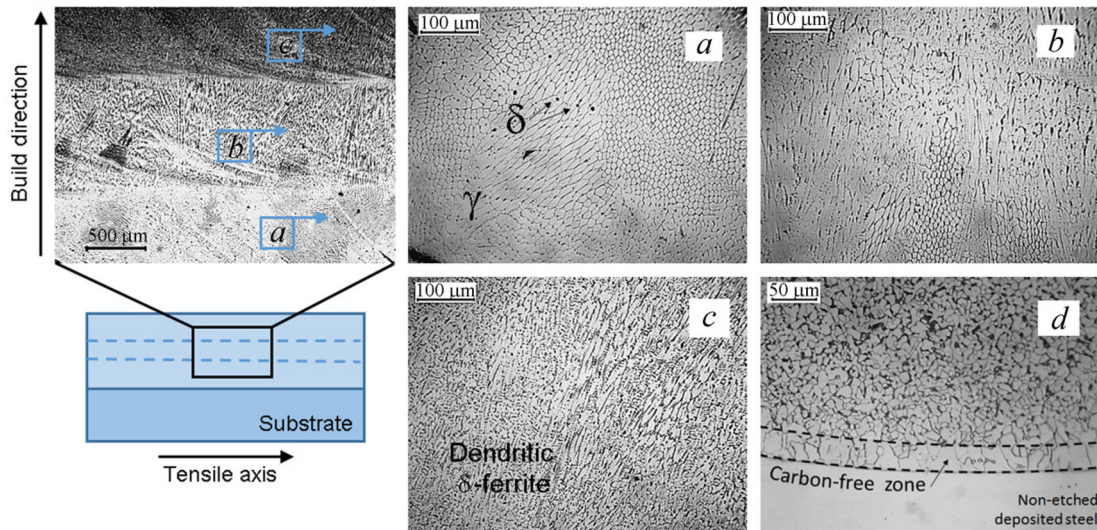
Fig. 2. Composite microstructure and diagram showing the characteristic areas of the specimen: the layer deposited after the first (*a*), second (*b*) and third beam pass (*c*) and the substrate (*d*).

first beam pass, fine-grained austenite is formed at the interface with the substrate, showing regions of honeycomb-shaped equiaxed grains ≈10 µm in size and elongated columnar grains with transverse dimensions of ≈50 µm (Fig. 2*a*). The grain boundaries are decorated with cellular δ-ferrite. At the next pass, colonies of δ-ferrite dendrites are formed in the austenitic matrix (Fig. 2*b* and *c*). The maximum ferrite fraction near the substrate is probably due to the highest cooling rate during layer formation and the influence of the carbon steel substrate. Metallographic analysis revealed decarburized zone with the width of $a \approx 50$ µm at the interface on the substrate side (Fig. 2*d*). The ferrite volume fraction distribution and the microhardness of the composite layers are shown in Fig. 3.

The stress-strain curves of the bimetal and its constituent metals obtained by conventional casting are shown in Fig. 4. According to Table 2, the AM composite has lower ductility and increased strength compared to the constituents. All stress-strain curves can be described by a parabolic function of the form $\sigma = \sigma_0 + K\varepsilon^n$, where K is the strain hardening coefficient and $n \leq 1$ is the strain hardening index. Depending on n, there are the yield plateau ($n = 0$), the linear strain hardening stage ($n = 1$), the parabolic strain hardening stage ($n = 0.5$), and the prefracture stage ($n \leq 0.5$) the duration of which is indicated in Table 2.

Local strain distribution

Autowave theory [10] states that plastic strain macrolocalization can change the autowave shape depending on the plastic flow stage. Lüders banding, typical for low-carbon steels and some other alloys, occurs within the yield plateau when the region of localized plastic deformation moves along the tensile axis. In this case, the Lüders fronts are switching autowaves that change the state of the deformed medium from the metastable (elastic) to stable (plastically deformed) one [11]. For homogeneous metallic materials, the kinetics of localized deformation in the parabolic hardening stage corresponds to a stationary periodic distribution of localization zones. The prefracture stage corresponds to the autowave collapse [9, 10].

Earlier we showed the presence of a yield plateau and a switching autowave during plastic deformation of an AM bimetal of two low-carbon steels [12]. Despite the entire composite remains ductile, Lüders banding in the deposited layer can be suppressed, implying the expansion of the localization area and a 35–40% lower strain rate than in the substrate. The Lüders fronts can begin splitting immediately after the band nucleation, and their propagation velocities can differ in different layers of the composite [12].
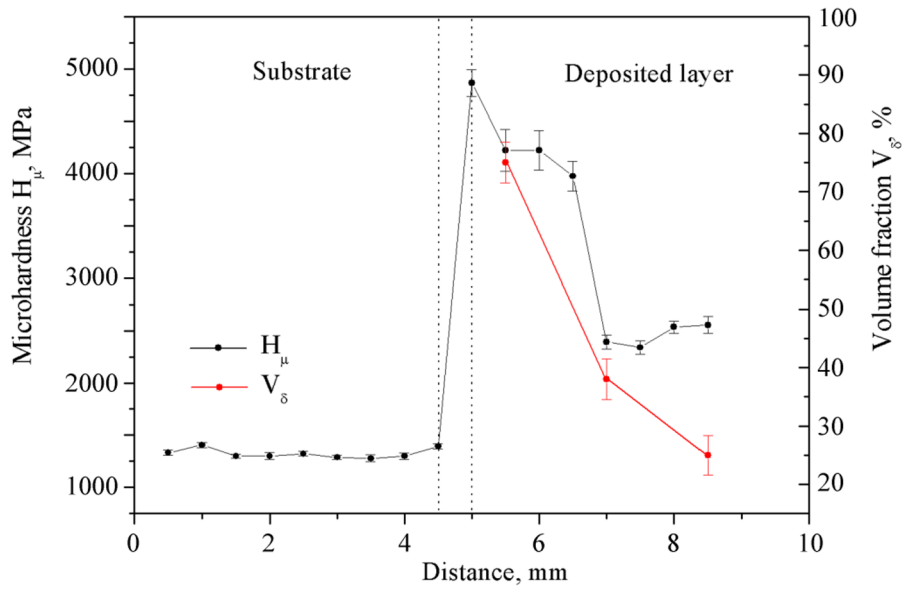
Fig. 3. Distribution of the microhardness and δ-ferrite volume fraction in the composite.
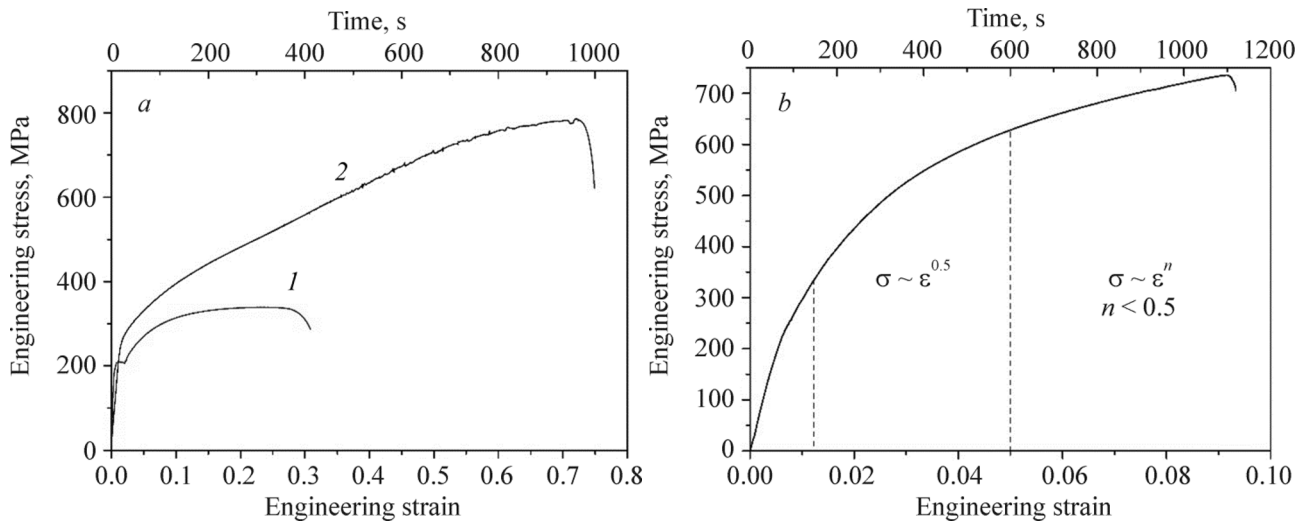

Fig. 4. Stress-strain curves for cast metals (*a*) and AM composites (*b*). Here curve *1*
is for the low-carbon steel, and curve *2* is for the austenitic stainless steel.

In work [13], in addition to the parabolic stage, a yield plateau was observed in the tensile curve of the laminate consisting of a carbon steel layer with top and bottom stainless steel coatings. Analysis of plastic strain localization patterns showed that the Lüders band in the low-carbon steel layer had two fronts moving at different velocities in opposite directions along the specimen axis. Thus, although a 750-µm thick cladding layer reduced the yield plateau length of the composite, it did not suppress Lüders deformation.

The curve of the studied composite has no yield plateau despite the large content of low-carbon steel (Fig. 4*b*). The propagation of the plastic deformation region as a Lüders band is not observed. The total distribution $\varepsilon_{xx}(x)$ within the parabolic stage in each bimetal layer is shown in Fig. 5*a*. Deformation occurs both in the substrate and in the deposited layer. One can see that stationary periodic distributions of localization zones with similar amplitudes are

TABLE 2. Mechanical Characteristics of the Materials and Total Strain Intervals Δε for the Plastic Flow Stages

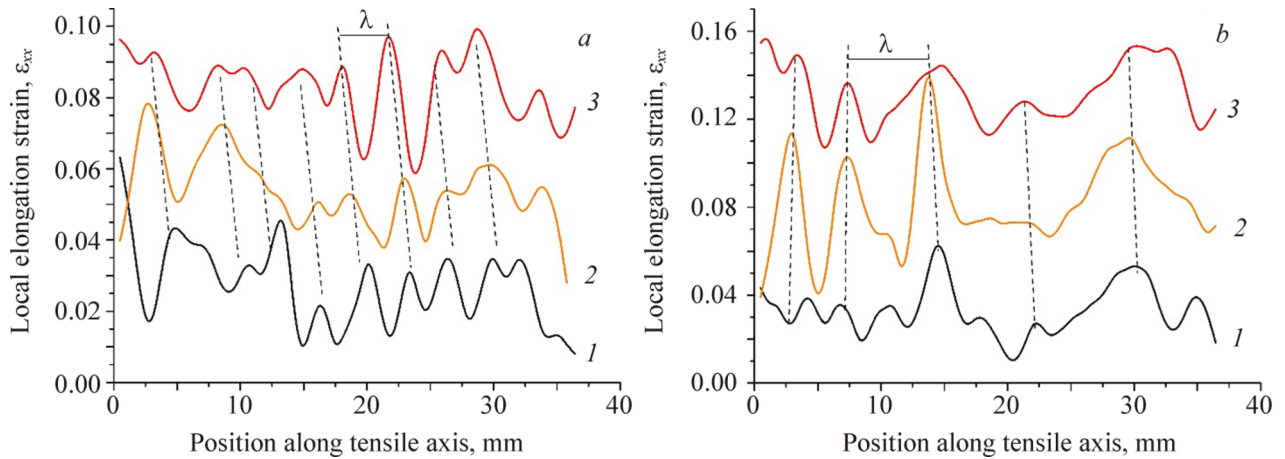| State	Yield point (MPa)	Tensile strength (MPa)	Elongation to failure	$n = 0$	$n = 1$	$n = 0.5$	$n \leq 0.5$
Low-carbon steel	209 ± 4.5	339 ± 4.5	0.30 ± 0.05	0.008–0.022	–	0.028–0.057	0.07–0.28
Austenitic stainless steel	262 ± 3.0	780 ± 5.0	0.70 ± 0.10	–	0.05–0.32	–	0.32–0.69
AM composite	226 ± 5.0	736 ± 3.5	0.09 ± 0.05	–	–	0.013–0.05	0.05–0.09

Fig. 5. Total elongation $\varepsilon_{xx}(x)$ at different stages in the bimetal layers. Here curves *1* are for the substrate, curves *2* are for the transition layer, and curves *3* are for the deposited metal (the curves are shifted by 0.03 along the *y* axis for clarity) at the parabolic (*a*) and prefracture stages (*b*).

formed throughout the deformation, like in homogeneous specimens. The localization period $\lambda = 3.7 \pm 0.4$ mm agrees with the period $3 \leq \lambda \leq 5$ mm for homogeneous specimens. The autowave model of plasticity interprets the system of equidistant immobile sites of localized plasticity at the parabolic stage as a stable dissipative structure [10].

Figure 5*b* shows the total distribution of the local strains $\varepsilon_{xx}(x)$ in the composite at the prefracture stage. There is an amplitude peak in the strain localization zone with the coordinate $x = 15$ mm in the transition layer. The position of the high-amplitude region coincides with the place of subsequent necking and fracture. Note that unlike ductile failure in homogeneous materials with a long prefracture stage (5–15%), where the deformation sites begin to move toward the high-amplitude stationary zone, the prefracture stage in the bimetal is short and shows the stationary distribution of deformation sites, as in the previous parabolic stage. However, the amplitude in some sites decreases, while the localization period increases to $\lambda = 6.5 \pm 0.5$ mm.

The curves of local strain accumulation near the fracture coordinate and in arbitrary regions in the substrate, transition zone, and deposited layer are shown in Fig. 6. At points $A'–C'$ near the fracture zone, starting from $t_{loc} = 930$ s ($\varepsilon = 7.6\%$), the local strain accumulation rate increases sharply in all bimetal layers (Fig. 6*a*). These values are even higher in the transition layer and deposited metal. The local strain accumulation rate from the beginning of deformation until t_{loc} can be determined by the slope of straight-line portions ($d\varepsilon_{int}/dt$) and is equal to $7.5 \cdot 10^{-5}$ s^{-1} in the substrate, $5.2 \cdot 10^{-5}$ s^{-1} in the transition layer, and $7.3 \cdot 10^{-5}$ s^{-1} in the deposited metal. After t_{loc}, the rate increases to $1.7 \cdot 10^{-4}$ s^{-1}, $2.9 \cdot 10^{-4}$ s^{-1}, and $2.2 \cdot 10^{-4}$ s^{-1}, respectively. At points $A–C$, the strains accumulate uniformly throughout the deformation (Fig. 6*b*). A crack is initiated at the fusion boundary between the substrate and deposited metal (Fig. 6*c*). Apparently,
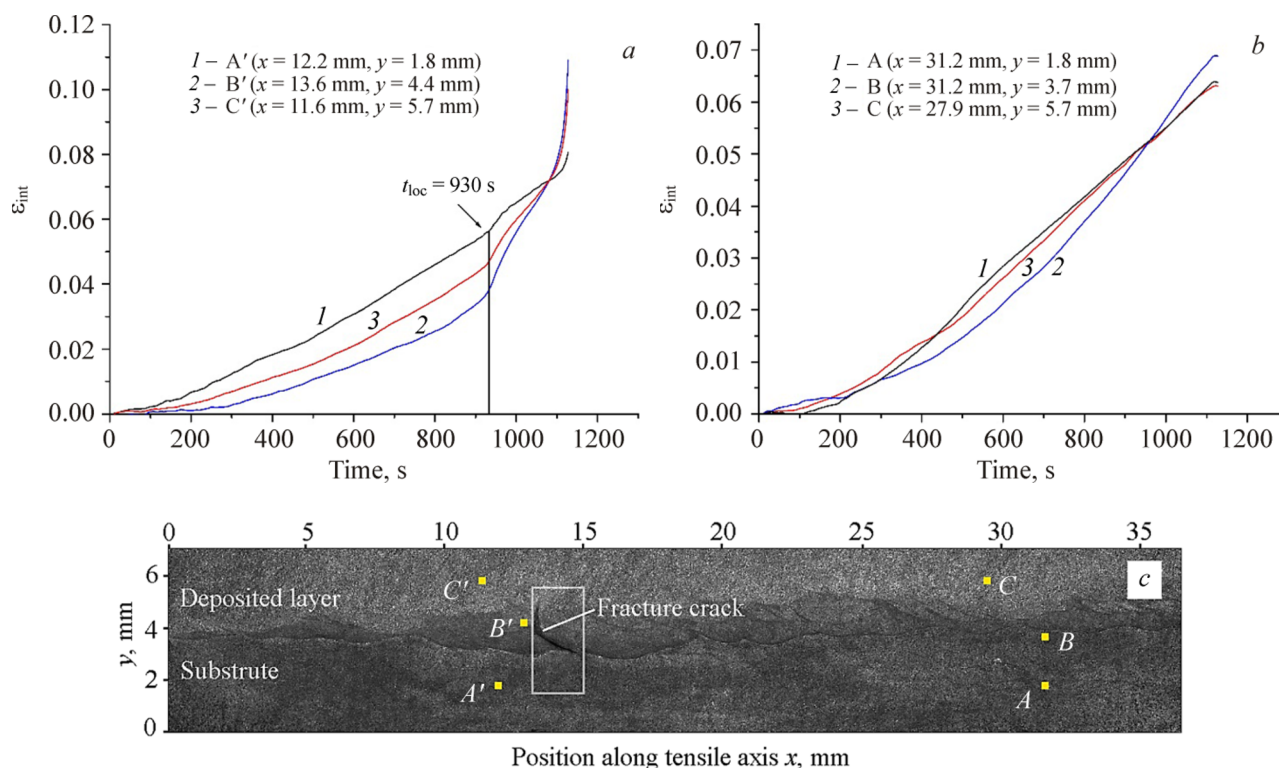
Fig. 6. Strain accumulation in the bimetal layers: (*a*) at points *A′*–*C′* near the fracture zone, (*b*) at arbitrary points *A*–*C*, (*c*) tensile specimen gauge section with the coordinates of points *A*, *A′* – substrate, *B*, *B′* – transition layer, and *C*, *C′* – deposited metal.

the fracture crack appears in the transition layer due to the carburized layer formation as result of carbon diffusion from the substrate to the deposited metal. The specimen fractured after 1127 s. Thus, the fracture site can be determined by the local strain distribution patterns at the prefracture stage at 14% strain before the ultimate strength is reached.

The study showed that Lüders banding is suppressed during deformation of low-carbon steel/stainless steel bimetal obtained by electron beam additive manufacturing. The plastic deformation of the bimetal is localized throughout the tensile stress-strain curve. First, the stationary dissipative system of localized plasticity foci is formed at the parabolic hardening stage with $n = 0.5$. At $n \leq 0.5$, the high-amplitude deformation zone is observed in the transition layer, which coincides with the site of future fracture. The location and time of the fracture can be determined by the local strain distribution pattern at the prefracture stage before visible necking.

REFERENCES

1. D. D. Gu, W. Meiners, K. Wissenbach, and R. Poprawe, Int. Mater. Rev., **57**, 133–164 (2012); http://dx.doi.org/10.1179/1743280411Y.0000000014.
2. S. Yu. Tarasov, A. V. Filippov, N. N. Shamarin, *et al.*, J Alloys Compd., **803**, 364–370 (2019); DOI: 10.1016/j.jallcom.2019.06.246.
3. G. L. Knapp, M. Gussev, A. Shyam, *et al.*, Addit. Manuf., **59**, 103150 (2022); https://doi.org/10.1016/j.addma.2022.103150.

4. E. G. Astafurova, M. Yu. Panchenko, V. A. Moskvina, *et al*., J. Mater. Sci., **55**, 9211–9224 (2020); https://doi.org/10.1007/s10853-020-04424-w.

5. M. A. Sutton, J. J. Orteu, and H. W. Schreier, Image Correlation for Shape, Motion and Deformation Measurements – Basic Concepts, Theory and Applications, Springer, Berlin (2009); https://doi.org/10.1007/978-0-387-78747-3.

6. J. D. Briers and S. Webster, Opt. Commun., **116**, 36–42 (1995); https://doi.org/10.1016/0030-4018(95)00042-7.

7. P. Margerit, D. Weisz-Patrault, K. Ravi-Chandar, and A. Constantinescu, Addit. Manuf., **37**, 101664 (2021); https://doi.org/10.1016/j.addma.2020.101664.

8. G. Mesmacque, Int. J. Impact Eng., **60**, 107–119 (2013); https://doi.org/10.1016/j.ijimpeng.2013.04.006.

9. L. B. Zuev, Bull. Russ. Acad. Sci. Phys., **78**, 957–964 (2014); DOI:10.3103/S1062873814100256.

10. L. B. Zuev, S. A.Barannikova, V. I. Danilov, and V. V. Gorbatenko, Prog. Phys. Met., **22**, 3–57 (2021); DOI: 10.15407/ufm.22.01.003.

11. V. I. Danilov, V. V. Gorbatenko, and L. V. Danilova, Steel Transl., **52**, 380–384 (2022); https://doi.org/10.3103/S0967091222040027.

12. M. V. Nadezhkin, D. V. Orlova, S. A. Barannikova, and L. B. Zuev, Key Eng. Mater., **910**, 849–856 (2022); https://doi.org/10.4028/p-jc90fe.

13. S. A. Barannikova and Y. V. Li, Russ. Phys. J., **63**, 731–737 (2020); https://doi.org/10.1007/s11182-020-02091-7.